Estimating Global and Regional Sea Level Trends within the Recent Climate Record

Sang-Ik Shin[1,2], Cécile Penland[2]†, Matthew Newman[2], and Michael A. Alexander[2]

[1]University of Colorado/CIRES, Boulder, Colorado, USA

[2]NOAA/Physical Sciences Laboratory, Boulder, Colorado, USA

Corresponding author: Sang-Ik Shin (sangik.shin@noaa.gov)

†Retired

Key Points:

- A new pattern-based method to isolate a trend with structure-like natural variability is applied to short global sea surface data records.
- The method can identify ensemble-mean forced trends within large climate model historical simulations from any single ensemble member.
- The observed sea level trend from 1993-2020 is everywhere positive, but its time series increases nonsteadily, pausing in the early 2000s.

Abstract

In this study, we introduce a pattern-based empirical approach to estimate externally-forced signals from short observational records based on applying Gram-Schmidt orthonormalization to the set of Empirical Normal Modes (ENMs) determined by a Linear Inverse Model (LIM). This procedure improves upon the LIM's least damped ENM (LDM) by removing its convolution with nonorthogonal modes of natural variability to represent the externally-forced signal. Applied to global sea level altimetry data, sea surface temperatures, and coastal tide gauge stations during the satellite observational era (1993-2020), this "optimized LDM" reveals a trend pattern that is everywhere positive, with higher values in the Pacific warm pool, Kuroshio-Oyashio extension, and the western portion of the North Atlantic basin. Coastal observations are consistent with this pattern, apart from a distinct vertical land motion signal. In contrast to previous analyses, however, we find no externally-forced sea level increase during the global warming "hiatus" period.

Plain Language Summary

In recent decades, coastal communities around the globe have experienced increasing frequency and severity of coastal flooding, raising the question of externally-forced signals' contribution to such risk. Our newly developed pattern-based method to identify the global and regional forced signals shows that observed sea levels rose globally from 1993 to 2020, but its rate paused in the early 2000s. The largest rise in coastal sea level occurs for tide gauge stations along the North American east coast, while high-latitude stations show a decrease in sea level compared to the rise of the nearby ocean. Such a decrease in coastal sea level indicates a strong upward land motion since the tide gauge station measures a relative sea level to the local reference.

1 Introduction

Global mean sea level rose in the 20th century at an unprecedented rate, which doubled in the past few decades [e.g., Hamlington et al., 2024]. Sea level change is neither spatially uniform nor linear in time, within either past observations [e.g., Fredrickse et al., 2020; Hamlington et al., 2022; Dangendorf et al., 2024] or future climate model projections [Bilbao et al., 2015; Fasullo and Nerem, 2018; IPCC, 2021]. These complex spatiotemporal changes will unevenly impact coastal communities around the globe by increasing the frequency and severity of flooding. Furthermore, uncertainties in how external forcing contributes to local sea level variations can impact the assessment of coastal flooding predictions made by operational seasonal forecast systems [Long et al., 2025]. Thus, identifying the externally-forced regional sea-level rise signals in both observations and models, especially along coastlines [e.g., Carson et al., 2016; Sweet et al., 2022], is critical for coastal planners and policymakers to anticipate sea-level impacts in their communities [e.g., Cazenave and Cozannet, 2014; Dusek et al., 2022].

Separating the externally-forced climate signals on global and regional scales from natural climate variability in short observational records is a critical challenge in climate dynamics [Solomon et al., 2011]. The fundamental issue is that natural climate variations can have spatial structures similar to those of the externally-forced pattern. To address this, two classes of global trend detection techniques have typically been employed: 1) direct estimation, or identifying a potentially nonlinear signal that, in some sense, evolves most slowly (e.g., a least damped dynamical mode [e.g., Penland and Matrosova, 2006; Solomon et al., 2011] or leading standing wave of the system [e.g., Vautard et al., 1992]); or 2) indirect estimation, in which the trend is determined as the remaining residual after identifying and removing modes of natural climate variability, often by using empirical orthogonal function (EOF) analysis [e.g., Ting et al., 2009; Wills et al., 2020]. However, EOFs represent the statistical decomposition of climate variability into an orthogonal set of patterns, which do not necessarily correspond to physical modes of climate dynamics [Monahan et al., 2009]. It may also be problematic to use EOFs in this manner if the pattern of externally-forced signals is not orthogonal to other natural climate modes.

These issues are particularly concerning for identifying forced sea-level rise signals over the altimetry era, when the amplitude of regional variations was considerably larger than that of the global mean trend [e.g., Zhang and Church, 2012; Han et al., 2017; Fasullo and Nerem, 2018]. To date, sea-level trends have generally been calculated using only the indirect estimation approach [e.g., Richter et al. (2020); Hamlington et al. (2022), Dangendorf et al. (2024), and references therein], typically by estimating natural variability with a small set of EOFs, removing them from the data, and then fitting the residual with low-order polynomials (e.g., linear or quadratic). Of course, there is no particular physical reason for the change in sea level to be so simple, but on the other hand, EOF orthogonality constraints make it challenging to isolate the time series of a more complex forced response.

In this study, we introduce a new empirical method that identifies the most slowly-varying spatial pattern, which we use to directly estimate global and regional sea-level trends over the relatively short, post-1993 satellite altimetry era from a combination of global SST and SSH fields and coastal tide gauge observations. Our approach is based upon the “least damped mode” (LDM) identified through linear inverse modeling [LIM; Penland and Sardeshmukh, 1995], which represents the system’s long-lasting standing wave; that is, the LIM eigenmode with the longest *e*-folding time [Penland and Matrosova, 2006]. For sufficiently long records, the LDM can provide a good estimate of the global SST trend component [e.g., Newman, 2007, 2013; Frankignoul et al., 2017], but for shorter records, it can mix with other LIM eigenmodes [Frankignoul et al., 2017]. Our new “optimized LDM” technique removes the effects of other eigenmodes from the LDM, which we demonstrate following the approach of Frankignoul et al. [2017], who compared techniques for identifying the externally-forced trend within a large ensemble [LENS; Deser et al., 2020] climate modeling framework. In a LENS, the ensemble mean can represent the externally-forced signal since averaging reduces noise (i.e., internal climate variability) variance by the factor of ensemble size [e.g., Rowell et al., 1995]. Then, trend-detection techniques are applied to each ensemble member separately, with the resulting trend estimates compared to the “known” forced signal.

2 Techniques used to determine trend patterns and associated time series

2.1 Least damped eigenmode of a LIM

In the LIM framework [Penland and Sardeshmukh, 1995], climate anomalies evolve as:

$$\frac{\mathrm{d}\mathbf{x}}{\mathrm{d}t} = \mathbf{L}\mathbf{x} + \boldsymbol{\eta}, \tag{1}$$

where $\mathbf{x}$ is the climate anomaly state vector, $\mathbf{L}$ is a deterministic feedback matrix, and all unpredictable dynamics are approximated as a stochastic forcing vector $\boldsymbol{\eta}$. The feedback matrix can be determined by $\mathbf{L} = \tau^{-1}\ln\left[\mathbf{C}(\tau)\mathbf{C}(0)^{-1}\right]$, where $\mathbf{C}(\tau) = \left\langle \mathbf{x}(t+\tau)\mathbf{x}(t)^{\mathrm{T}} \right\rangle$ is the lag covariance matrix at time lag τ. The empirical normal modes (ENMs; eigenvectors of $\mathbf{L}$; e.g., Penland and Sardeshmukh [1995]; von Storch et al. [1995]), their associated eigenvalues, and their adjoints (eigenvectors of $\mathbf{L}^{\mathrm{T}}$) define the deterministic feedback matrix $\mathbf{L}$. Then, any state can be expressed as a sum over the ENMs:

$$\mathbf{x}(t) = \sum_{j}^{n} c_j \exp(\beta_j t)\mathbf{u}_j = \sum_{j}^{n} z_j(t)\mathbf{u}_j, \tag{2}$$

where c_j is a complex constant that depends upon the initial state, $\mathbf{u}_j$ is the *j*-th ENM, and β_j is the corresponding eigenvalue. $z_j(t) = c_j \exp(\beta_j t) = \mathbf{v}_j^{\mathrm{T}}\mathbf{x}(t)$ is the *j*-th ENM time series, and $\mathbf{v}_j$ is the *j*-th adjoint vector that satisfies $\mathbf{u}\mathbf{v}^{\mathrm{T}} = \mathbf{I}$. The decay time and oscillation period of each ENM are $-1/\mathrm{Re}(\beta_j)$ and $2\pi/\mathrm{Im}(\beta_j)$, respectively.

Many studies using relatively long SST and SSH records have found that the LDM, the ENM with the longest decay time [e.g., Penland and Matrosova, 2006], can provide a good estimate of the trend component [e.g., Newman, 2007, 2013; Solomon et al., 2011; Frankignoul et al., 2017; Shin and Newman, 2022]. However, Frankignoul et al. [2017] noted that the LDM can be sensitive to record length, such that in a relatively short record, the LDM decay time is not always well separated from those of other ENMs (Fig. S1). Consequently, the externally-forced signal could project onto several ENMs, and conversely, the LDM could represent both the externally-forced signal and natural climate variability with a similar spatial structure.

To address this, we aim to remove all contributions of natural climate variability upon the LDM time series. First, rewrite (2) as:

$$\mathbf{x}(t) = z_1(t)\mathbf{u}_1 + \sum_{j=2}^{n} z_j(t)\mathbf{u}_j \,, \tag{3}$$

where $\mathbf{u}_1$ is the LDM and its expansion coefficient time series is $z_1(t)$. To estimate the contribution from all other modes to LDM, we regress the LDM onto all other ENMs and subtract the residual. This was done by defining an adjusted LDM adjoint vector, $\mathbf{v}_1^*$, as

$$\mathbf{v}_1^* = \mathbf{v}_1 - \mathbf{V}\gamma \,, \tag{4}$$

where $\mathbf{V}$ is the adjoint submatrix containing all adjoint vectors other than the LDM, and $\gamma = (\mathbf{V}^{\mathrm{T}}\mathbf{V})^{-1}\mathbf{V}^{\mathrm{T}}\mathbf{v}_1$ is a vector of multiple linear regression coefficients. Then, the optimized forced signal becomes,

$$\mathbf{x}_{\mathrm{F}}(t) = z_1^*(t)\mathbf{u}_1 = \mathbf{v}_1^{*\mathrm{T}}\mathbf{x}(t)\mathbf{u}_1 = (\mathbf{v}_1 - \mathbf{V}\gamma)^{\mathrm{T}}\mathbf{x}(t)\mathbf{u}_1 \,. \tag{5}$$

This procedure is known as Gram-Schmidt orthonormalization [Gram, 1883; Schmidt, 1907; and also, e.g., Strang, 2016]. As a result, the adjusted adjoint vectors become orthogonal; thus, the ENM time series $z_j^*(t)$ are uncorrelated, while the ENM patterns remain nonorthogonal. We refer to the results of this approach [$z_1^*(t)$ and $\mathbf{u}_1$] as the "optimized LDM" (O-LDM).

2.2 Multi-channel singular spectrum analysis

We compare the O-LDM to multi-channel singular spectrum analysis (MSSA), formally equivalent to Extended EOF analysis [e.g., Weare and Nasstrom, 1982], where the data matrix contains values measured at different locations and different time lags. Thus, with the state vector $\mathbf{x}$ (*M* locations x *N* times), the data matrix $\mathbf{X}$, whose dimension is $M(l+1) \times (N-l)$, is:

$$\mathbf{X} = \begin{bmatrix} \mathbf{x}(1) & \mathbf{x}(2) & \ldots & \mathbf{x}(N-l) \\ \mathbf{x}(2) & \mathbf{x}(3) & \ldots & \mathbf{x}(N-l+1) \\ \ldots & \ldots & \ldots & \ldots \\ \mathbf{x}(l+1) & \mathbf{x}(l+2) & \ldots & \mathbf{x}(N) \end{bmatrix}, \tag{6}$$

where l is the predefined lag equivalent to the width of a moving window passed through the time series. The eigenanalysis of $\mathbf{C} = \mathbf{X}\mathbf{X}^{\mathrm{T}}$ yields the orthogonal MSSA patterns and associated uncorrelated time series. Then, the time series with the longest decorrelation time scale and its associated pattern represents the forced signal of the system.

Again, MSSA results could also be sensitive to a short record by mixing some natural climate variability with an externally-forced trend so that the MSSA EOFs do not sufficiently separate between distinct oscillations [Groth and Ghil, 2011]. This issue may be addressed by rotating the MSSA EOFs via Varimax Rotation [Groth and Ghil, 2011] so that the forced signal pattern is no longer orthogonal to other climate variations. We refer to the resulting adjusted MSSA as O-MSSA.

3 Datasets and method details

3.1 Datasets

Both techniques are evaluated using gridded output from large ensembles (LENS) of historically forced coupled model simulations. We use SSTs covering the period 1959-2013 from two LENS datasets: the 30-member ensemble SPEAR-LE [Delworth et al., 2020] and the 40-member ensemble CESM1-LE [Kay et al., 2015]. These LENS simulations include forcings due to greenhouse gases, aerosols, etc. [Deser et al., 2020]. All gridded data were interpolated to a common 2°×2° in the longitudinal and latitudinal direction over the ice-free global ocean.

The gridded observational datasets are monthly averaged sea surface temperatures (SSTs) from HadISST [Rayner et al., 2003] during 1901-2020 and sea surface heights from AVISO (https://doi.org/10.48670/moi-00148) during 1993-2020. Monthly sea level observations at 397 tide gauge stations during 1993-2020 from the PSMSL (Permanent Service for Mean Sea Level) database [Woodworth and Player, 2003] are also used.

3.2 LDM details

For the SST-only analyses, we applied a three-month running-mean smoother to capture ocean memory effects. We retained the leading 18 EOFs of the SST anomalies, defined by removing the mean annual cycle, which explains about 77% of the total variance. The corresponding principal component (PC) time series then comprises the LIM state vector $\mathbf{x}$. We used a 3-month training lag to determine the LIM and the LDM.

For the analysis of sea level during 1993-2020, we first performed a combined EOF analysis of global SSH and tide gauge sea-level anomalies to reduce degrees of freedom. We retained the leading 14 SST and 12 {SSH, sea level} EOFs of monthly anomalies, explaining about 67% and 50% of the total variance, respectively. Then $\mathbf{x}$ consists of the corresponding PCs:

$$\mathbf{x} = \begin{bmatrix} \text{SST} \\ \{\text{SSH, sea level}\} \end{bmatrix}. \quad (7)$$

For this LIM, we did not apply a running mean to the monthly anomalies since SSH provides the necessary ocean memory effects [e.g., Newman et al., 2011], and likewise, we used a 1-month training lag.

3.3 MSSA details

For MSSA, we used the same EOFs and PCs used for the LIM. Optimal values for the lag l are $(\ln N)^m$ with $m \in (1.5, 3)$ [Khan and Poskitt, 2011]. A 100-year monthly data set l can range from 18.9 to 356.4 months, allowing analysis of quasi-oscillatory structures with periods in the range $(0.2l,\ l)$ [Vautard et al., 1992]. Here, l is set to 84 months, but our results are not sensitive to a choice of l longer than 36 months and shorter than 240 months.

4 Evaluation of Optimized LDM and MSSA

4.1 SST trend detection in LENS output

We start by applying the O-LDM and O-MSSA techniques to each SPEAR (CESM) LENS ensemble, yielding 30 (40) different estimates of the trend pattern and its time series. Recall that the success of either technique is measured by how well its application to a *single* ensemble member captures the *ensemble-mean* pattern and its time series, which should represent the externally-forced model response [Frankignoul et al., 2017].

For the SPEAR-LE (Fig. 1a), both the O-LDM (red) and O-MSSA (blue) time series generally capture the temporal evolution of the globally-averaged ensemble mean forced response (black), although the O-MSSA is notably smoother. However, this smoothness may be misleading since, in contrast to the O-LDM and the globally-averaged ensemble mean, the O-MSSA time series do not resolve the sudden cooling in the 1960s and 1990s, which are thought to be externally-forced responses to large volcanic eruption-induced stratospheric sulfate aerosol changes [e.g., Robock et al., 1999]. Still, for both techniques, the ensemble-mean forced response pattern (Fig. 1b) correlates very highly with the trend patterns determined separately for each ensemble member (Fig. 1c).

The overall picture for the CESM1-LE is similar, with the O-LDM generally capturing the ensemble-mean forced response, while O-MSSA is similar but much smoother and misses the sudden cooling events (Fig. 1d). There is a lower signal-to-noise ratio (forced response compared to natural climate variability) in the CESM1-LE compared to the SPEAR-LE, principally due to much stronger ENSO variability in the CESM1 (e.g., Amaya et al., 2025). As a result, the O-MSSA has many ensemble members for which the leading EOF and accompanying time series represent ENSO. For these cases, we identify the externally-forced component with the slowest decorrelating time series (and EOF), which is in a higher order mode (Fig. 1f; open circles).

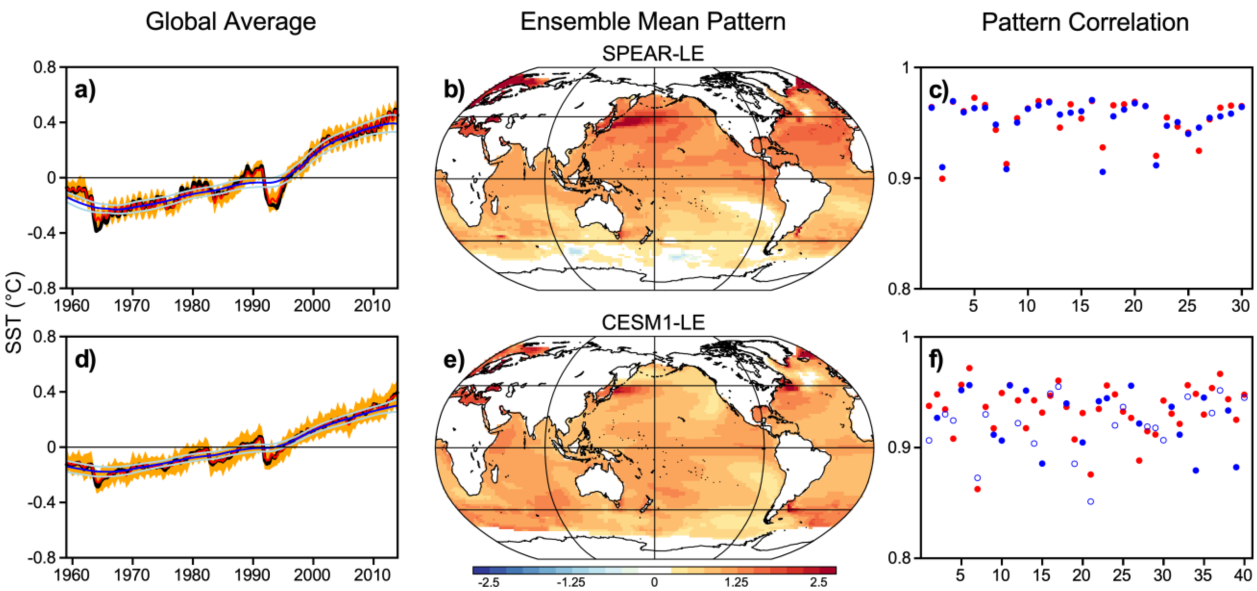

Figure 1. **a**) The globally-averaged externally-forced signals in the 30-member SPEAR-LE derived from the O-LDM (red) and O-MSSA (blue) for the period 1959-2013. The mean and ±1 standard deviation of the time series determined from each ensemble member are shown as red (blue) and orange (light blue), respectively, for the O-LDM (O-MSSA). The globally-averaged ensemble-mean SST anomalies are also shown as thick black lines. **b**) The pattern associated with the globally-averaged ensemble-mean SST anomaly time series. **c**) Pattern correlations (ranging between 0.8 and 1) between the ensemble-mean pattern in (b) and the eigenmode pattern associated with each ensemble member's external forcing response for the O-LDM (red dots) and O-MSSA (blue dots; open circle when a higher order mode is chosen). (**d-f**) the same as (a-c) but for the 40-member CESM1-LE.

We next test whether the O-LDM can generate consistent results with a record length similar to satellite datasets by determining the trend from each ensemble member using only the last 28 years (1986-2013) of the SPEAR-LE ensemble. Figure 2a shows the globally-averaged ensemble-mean forced response compared to the mean and ±1 standard deviation of 30 O-LDM estimates using each ensemble member, and Fig. 2b shows the associated ensemble-mean forced response pattern. The excellent comparisons between Fig. 2a and the 1986-2013 period in Fig. 1a, and between the associated ensemble-mean patterns in Figs. 1b and 2b, demonstrate how well the O-LDM captures the evolution of the forced response regardless of the length of the record.

One key assumption made in the O-LDM technique (and many others, including O-MSSA) is that the trend pattern is fixed over the entire data record, or at least its change over time is negligible relative to the variations of its associated time series, as appears the case in Figs. 2ab. To investigate this assumption further, we estimated ensemble-mean forced responses of SPEAR-LE over different time intervals, starting with 1959-2013 and continuing with 1961-2013, 1963-2013, and so on up to 2007-2013. For each period, the anomalies are defined relative to the same 1959-2013 climatological annual cycle, ensuring that the trend is relative to a consistent benchmark. Figure 2c shows that the trend pattern determined for each year range is always highly correlated with the 1959-2013 ensemble-mean pattern (Fig. 1b). Also, the globally-averaged forced signals and accompanying patterns in all 25 cases converge to virtually the same forced response determined from longer records, both in amplitude and in stationarity of the global response time series (see inset in Fig. 2c). Together, these both suggest that the forced pattern could indeed be relatively unchanging.

4.2 SST trend detection in observations

We now apply the LDM and MSSA techniques to estimate the externally-forced signal in observed (HadISST) monthly SST anomalies over the ice-free ocean for long (1901-2020) and (comparatively) short (1961-2020) records. For the long record, the globally-averaged time series derived from the LDM (red) and MSSA (blue) techniques are all similar to the observed globally-averaged SST anomaly time series (gray shading), as shown in Fig. 3a. Note that, again, the MSSA time series is much smoother than both the LDM and global-mean SST time series. However, for the short record (Fig. 3b), neither the LDM nor MSSA matches the global mean time series. Moreover, the LDM time series in Fig. 3b differs from the LDM time series over the 1961-2020 period in Fig. 3a, demonstrating that the LDM does not provide a consistent estimate of the forced signal.

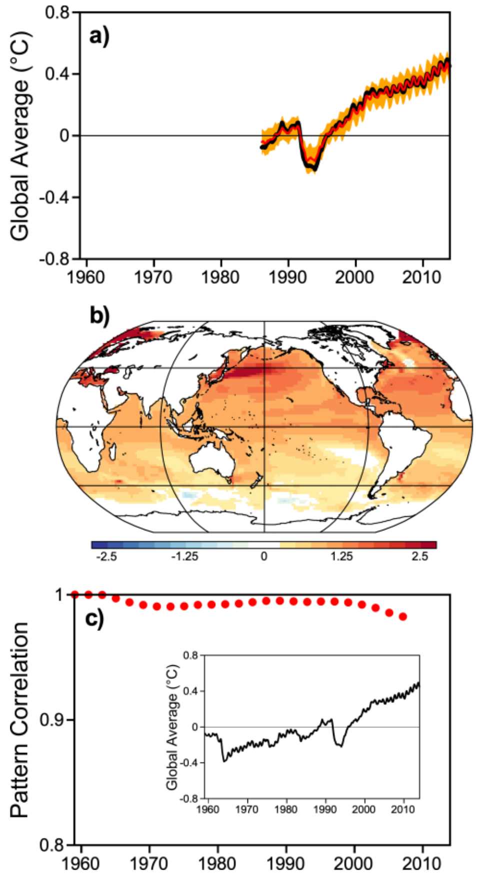

Figure 2. Comparison of SPEAR-LE ensemble means over different periods. **a)** Same as Fig. 1a but for the period 1986-2013. **b**) Same as Fig. 1b but for the period 1986-2013. **c)** The pattern correlation between the ensemble-mean forced response pattern derived from the SPEAR-LE for the period 1959-2013 (that is, Fig. 1b) with the ensemble-mean forced response pattern derived over the periods 1959-2013, 1961-2013, 1963-2013, and so on up to 2007-2013. The inset shows the corresponding time series determined separately for each period. In all cases, the anomalies are defined relative to the 1959-2013 climatological annual cycle.

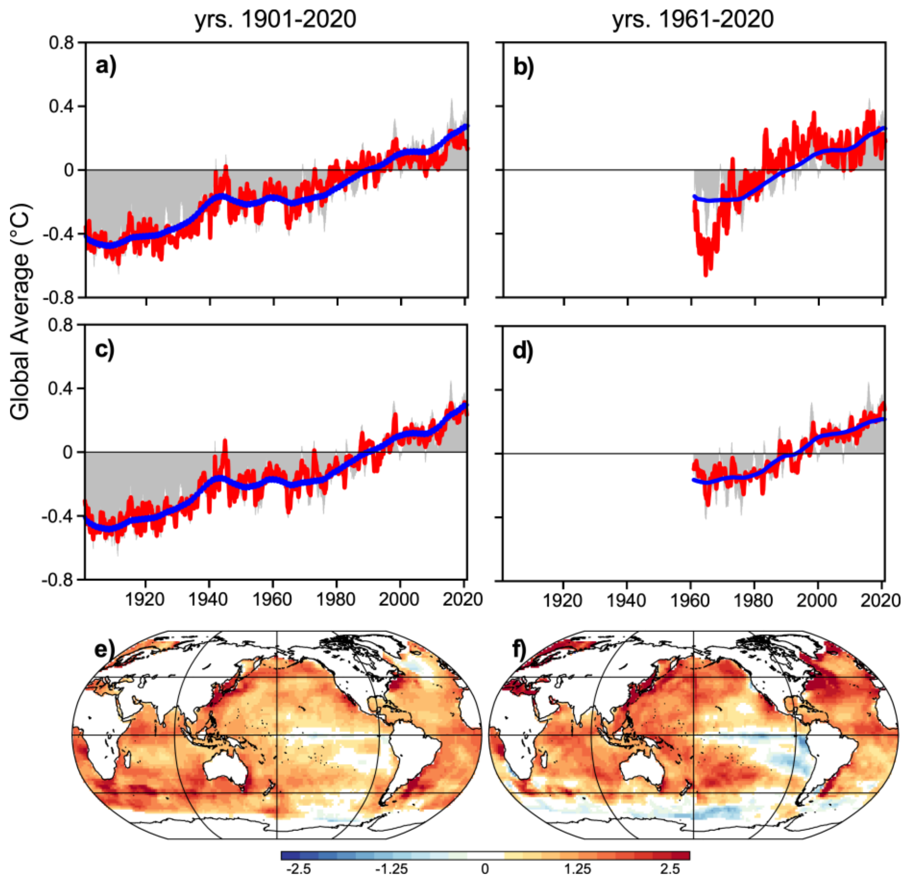

Figure 3. Trend analysis for HadISST SST dataset. **a-b)** The globally-averaged externally-forced signals derived from the LDM (red) and MSSA (blue), compared with the observed globally-averaged SST time series (gray shading) for a) 1901-2020 and b) 1961-2020. **c-d)** Same as (a-b) but using the O-LDM (red) and O-MSSA (blue) for c) 1901-2020 and d) 1961-2020. **e-f)** The associated eigenmode pattern of the O-LDM for e) 1901-2020 and f) 1961-2020.

In contrast, the optimized techniques, O-LDM and O-MSSA, are more consistent within the 1961-2020 period for both the long (Fig. 3c) and short (Fig. 3d) observational records and are also more consistent with the globally-averaged SST. The associated eigenmode patterns for the O-LDM (Figs. 3e and f), which are highly correlated (r=0.99) for both periods with the O-MSSA estimates, show warming over most of the oceans except for the eastern tropical Pacific and Northeast Atlantic regions, as noted in earlier studies (e.g., Compo and Sardeshmukh, 2010; Solomon and Newman, 2012). Note that both O-LDM time series have the same stair-step shape, with periods when the trend pattern slows its increase, roughly between 1940-1975 and 2003-2012.

5 Observed Forced Sea Level Rise Signals

Finally, we use the O-LDM to estimate the externally-forced sea level signal over the 1993-2020 period. The globally-averaged time series associated with the O-LDM pattern is shown in Fig. 4a.

The accompanying patterns of SST, SSH, and coastal sea level are in Fig. 4b, c, and d, respectively. By design, they share the same time series but with different amplitudes. Note that this time series is distinguishable from low-order polynomials such as linear and quadratic expressions. In particular, even over this relatively short period, the externally-forced signal has not constantly increased; instead, it slowed from about 2003 to 2012 and accelerated thereafter.

The largest externally-forced signal of coastal sea level occurs for tide gauge stations along the North American east coast (Fig. 4d). Interestingly, high latitude stations show negative forced signals in contrast to positive responses in the nearby ocean (Fig. 4c). This is because tide gauge station observations are relative to the local reference, which is discerned from the mean sea level in the SSH dataset. Thus, the negative responses in high latitudes indicate strong positive vertical land motion (e.g., Fig. 10 of Hammond et al. [2021]).

Next, we removed the estimated externally-forced signal from observations by determining the trend component from eqn. (5), that is, multiplying the Figs. 4b-d patterns by the Fig. 4a time series. Figs. 4e-i compares the full and detrended time series for a few selected tide gauge stations along the U.S. West (San Francisco and San Diego), East (Charleston and Boston), and Gulf (Galveston) Coasts. For all five stations shown (as well as the remaining stations), removing the trend component yields a filtered time series with no apparent upward or downward trend. Notably, specific variations in Fig. 4a are evident for each station, including the early 2000s trend slowdown.

Additionally, we compared EOFs (Fig. S2) and PCs (Fig. S3) from the original and detrended global SSH anomalies. While the leading original SSH EOF (Fig. S2a) is very similar to the LDM's SSH component (Fig. 4c), its associated PC increases almost linearly, in contrast to the O-LDM time series (Fig. 4a). The difference arises because the second original SSH EOF does not represent purely internal variability: Although this EOF is dominated by a mature ENSO pattern (Fig. S2b, in its El Niño phase), it also includes a contribution from the global trend pattern (Fig. S4), which is only removed by detrending with the O-LDM (Fig. S2e). In contrast, the next several original EOFs and associated PCs are nearly identical to their detrended counterparts (Figs. S2c/S3c with S2f/S3f and S2d/S3d with S2g/S3g).

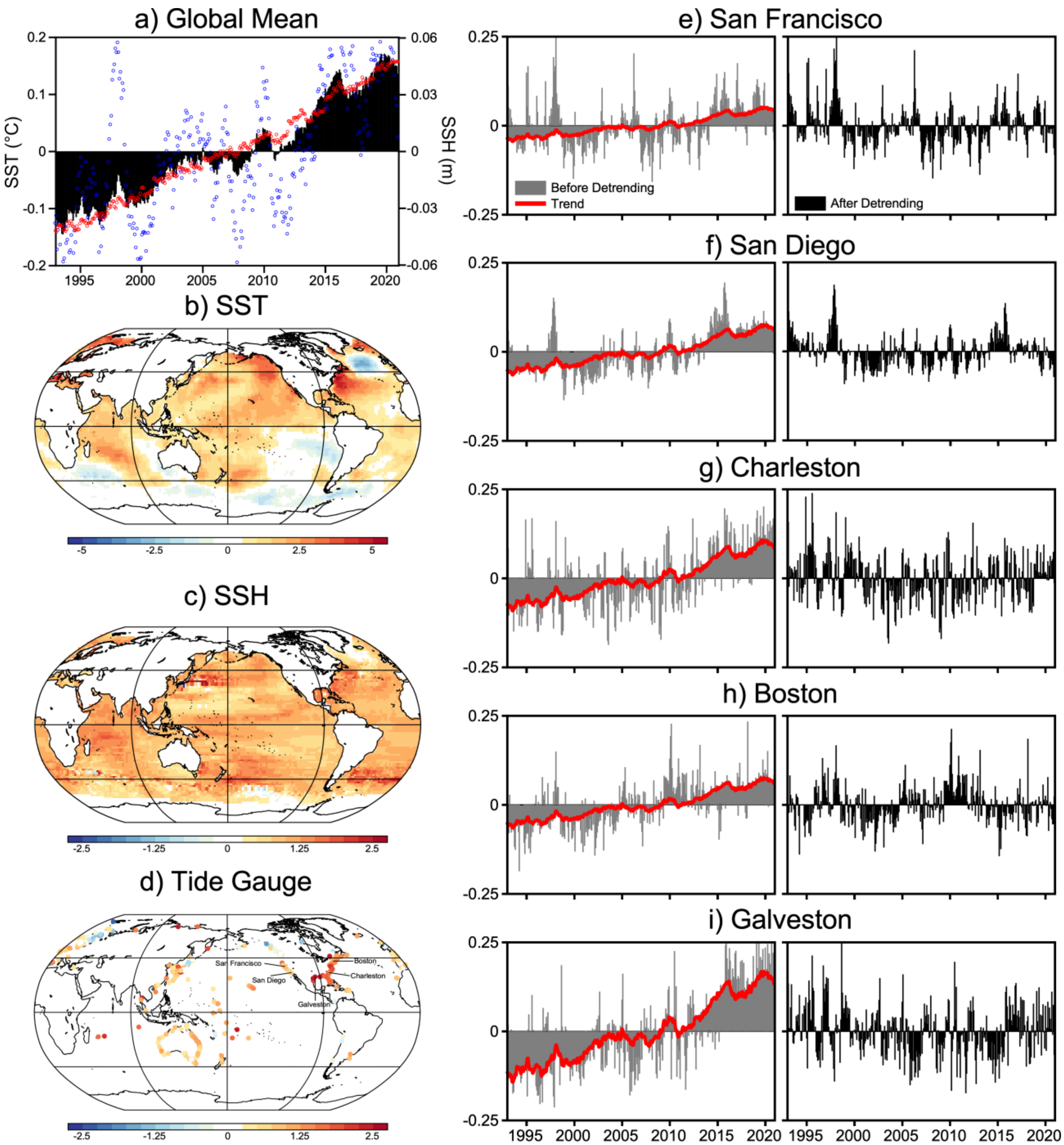

Figure 4. a) The globally-averaged externally-forced signals of SST (in ºC) and SSH (in m) derived from the O-LDM for 1993-2020. Blue (red) dots indicate monthly global-mean SST (SSH) anomalies. **b-d)** The associated patterns for **b)** SST**, c)** sea level at the tide gauge stations, and **d)** SSH**. e-i)** The (left) unfiltered and (right) filtered sea level time series in m at the selected tide gauge locations, **e)** San Francisco, **f)** San Diego, **g)** Charleston, **h)** Boston, and **i)** Galveston. The externally-forced responses from the O-LDM are also shown as thick red lines in the left panels.

6 Conclusions

This study introduced a new pattern-based empirical method to estimate externally-forced signals over relatively short observational periods. Gram-Schmidt orthonormalization is used to remove the projection of other ENMs, with similar structures and decay times, upon the LIM's LDM so that the resulting optimized LDM represents the external forced signal. We find that the optimized LDM can successfully estimate forced signals within CESM1 and SPEAR LENS simulations from a single model ensemble member with only a few decades of data. Considering that the ENMs form a nonorthogonal set and that nonorthogonal EOF rotation is also necessary for MSSA to identify forced signals in a short record, we conclude that the forced signal pattern is not orthogonal to other climate variability. Note, however, that to the extent the forced pattern may not change with time (e.g., Fig. 2) and can be identified as a LIM eigenmode, it can still be considered *independent* of natural climate variations.

While the global pattern of sea level change that we find is consistent with several previous studies, its associated time series is not since it does not vary smoothly and, therefore, is not well characterized by simple linear or quadratic fits. In particular, we do not find an obvious increase in the externally-forced signal of sea level change during the early 2000s global hiatus period. Note that our estimate captures changes in altimetric sea level and tide gauge sea level, which can differ due to vertical land motion that might also be calculable from our results.

The O-LDM time series is also less smooth than many other trend-estimation techniques, such as the O-MSSA (Figs. 1 and 3). This could be an *advantage* of the O-LDM technique, at least in part: Recall that it was better able to capture sudden cooling events from single ensemble members in the LENS simulations (Fig. 1). Still, how much of the small high-frequency variability reflects fast variations in the forced response, as opposed to noise, remains to be determined.

Acknowledgments

S.S. and M.N. acknowledge support from NOAA Cooperative Agreement NA22OAR4320151 and the U.S. DOC/NOAA/Bipartisan Infrastructure Law (BIL). The authors wish to thank Billy Sweet for his helpful feedback.

Open Research

All detrended monthly tide gauge data is available at https://github.com/Sang-Ik-Shin/Sea-Level-Trend.

References

Amaya, D. J., Maher, N., Deser, D., Jacox, M. G., Alexander, M., Newman, M., et al. (2025). Linking projected changes in seasonal climate predictability and ENSO amplitude. Journal of Climate, 38(3), 675-688. https://doi.org/10.1175/JCLI-D-23-0648.1

Bilbao, R. A. F., Gregory, J. M., & Bouttes, N. (2015). Analysis of the regional pattern of sea level change due to ocean dynamics and density change for 1993–2099 in observations and CMIP5 AOGCMs. Climate Dynamics, 45, 2647–2666. https://doi.org/10.1007/s00382-015-2499-z

Boiseau, M., Ghil, M., & Julliet-Leclerc, A. (1999). Climatic trends and interdecadal variability from South-Central Pacific coral records. Geophysical Research. Letters, 26(18), 2881-2884. https://doi.org/10.1029/1999GL900595

Carson, M., Köhl, A., Stammer, D., Slangen, A. B. A., Katsman, C. A., van de Wal, R. S. W., et al. (2016). Coastal sea level changes, observed and projected during the 20th and 21st century. Climatic Change, 134, 269–281. https://doi.org/10.1007/s10584-015-1520-1

Cazenave, A., & Cozannet, G. L. (2014). Sea level rise and its coastal impacts. Earth's Future, 2, 15-34. https://doi.org/10.1002/2013EF000188

Compo, G. P., & Sardeshmukh, P. D. (2010). Removing ENSO-related variations from the climate record. Journal of Climate, 23(8), 1957-1978. https://doi.org/10.1175/2009JCLI2735.1

Dangendorf, S., Sun, Q., Wahl, T., Thompson, P., Mitrovica, J. X., & Hamlington, B. (2024). Probabilistic reconstruction of sea-level changes and their causes since 1900. Earth System Science Data, 16, 3471–3494. https://doi.org/10.5194/essd-16-3471-2024

Delworth, T. L., Cooke, W. F., Adcroft, A., Bushuk, M., Chen, J.-H., Dunne, K. A., et al. (2020). SPEAR: The next generation GFDL modeling system for seasonal to multidecadal prediction and projection. Journal of Advances in Modeling Earth Systems, 12(3), e2019MS001895. https://doi.org/10.1029/2019MS001895

Deser, C., Lehner, F., Rodgers, K. B., Ault, T., Delworth, T. L., DiNezio, P. N., et al. (2020). Insights from Earth system model initial-condition large ensembles and future prospects. Nature Climate Change, 10, 277–286, https://doi.org/10.1038/s41558-020-0731-2

Dusek, G, Sweet, W. V., Widlansky, M. K., Thompson, P. R., & Marra, J. J. (2022). A novel statistical approach to predict seasonal high tide flooding. Frontiers in Marine Science, 9, 1073792. https://doi.org/10.3389/fmars.2022.1073792

Farrell, B. (1988). Optimal excitation of neutral Rossby waves. Journal of the Atmospheric Sciences, 45(2), 163–172. https://doi.org/10.1175/1520-0469(1988)045<0163:OEONRW>2.0.CO;2

Fasullo, J. T., & Nerem, R. S. (2018). Altimeter-era emergence of the patterns of forced sea-level rise in climate models and implications for the future. Proceedings of the National Academy of Sciences, 115(51), 12944–12949. https://doi.org/10.1073/pnas.1813233115

Frankignoul, C., Gastineau, G., & Kwon, Y.-O. (2017). Estimation of the SST response to anthropogenic and external forcing and its impact on the Atlantic multidecadal oscillation and the Pacific decadal oscillation. Journal of Climate, 30(24), 9871–9895. https://doi.org/10.1175/JCLI-D-17-0009.1

Frederikse, T., Landerer, F., Caron, L., Adhikari, S., Parkes, D., Humphrey, V. W., et al. (2020). The causes of sea-level rise since 1900, Nature, 584, 393–397. https://doi.org/10.1038/s41586-020-2591-3

Gram, J. P. (1883). Ueber die Entwickelung reeler Funktionen en Reihen mittelst der kleinsten Quadrate. Journal für die Reine und Angewandte Mathematik, 94, 41-73.

Groth, A., & Ghil, M., (2011). Multivariate singular spectrum analysis and the road to phase synchronization. Physical Review E, 84, 036206. https://doi.org/10.1103/PhysRevE.84.036206

Hamlington, B. D., Fasullo, J. T., Nerem, R. S., Kim, K., & Landerer, F. W. (2019). Uncovering the Pattern of Forced Sea Level Rise in the Satellite Altimeter Record. Geophysical Research Letters, 46(9), 4844–4853. https://doi.org/10.1029/2018gl081386

Hamlington, B. D., Chambers, D. P., Frederikse, T., Dangendorf, S., Fournier, S., Buzzanga, B., et al. (2022). Observation-based trajectory of future sea level for the coastal United States tracks near high-end model projections. Nature Communications Earth & Environment, 3, 230. https://doi.org/10.1038/s43247-022-00537-z

Hamlington, B. D., Bellas-Manley, A., Willis, J. K., Fournier, S., Vinogradova, N., Nerem, S., et al. (2024). The rate of global sea level rise doubled during the past three decades. Nature Communications Earth & Environment, 5, 601. https://doi.org/10.1038/s43247-024-01761-5

Hammond, W. C., Blewitt, G., Kreemer, C., & Nerem, R. S. (2021). GPS imaging of global vertical land motion for studies of sea level rise. Journal of Geophysical Research: Solid Earth, 126, e2021JB022355. https://doi.org/10.1029/2021JB022355

Han, W., Meehl, G. A., Stammer, D., Hu, A., Hamlington, B. D., Kenigson, J., et al. (2017). Spatial patterns of sea level variability associatedwith natural internal climate modes. Surveys in Geophysics, 38(1), 217–250. https://doi.org/10.1007/s10712-016-9386-y

IPCC, 2021: Climate Change 2021: The Physical Science Basis. Contribution of Working Group I to the Sixth Assessment Report of the Intergovernmental Panel on Climate Change [Masson-Delmotte, V., P. Zhai, A. Pirani, S.L. Connors, C. Péan, S. Berger, N. Caud, Y. Chen, L. Goldfarb, M.I. Gomis, M. Huang, K. Leitzell, E. Lonnoy, J.B.R. Matthews, T.K. Maycock, T. Waterfield, O. Yelekçi, R. Yu, and B. Zhou (eds.)]. Cambridge University

Press, Cambridge, United Kingdom and New York, NY, USA, 2391 pp. https://doi.org/10.1017/9781009157896

Khan, M. A. R., & Poskitt, D. S. (2011). Window length selection and signal-noise separation and reconstruction in singular spectrum analysis. Monash Econometrics and Business Statistics Working Papers 23/11, Monash University, Department of Econometrics and Business Statistics.

Kay, J. E., Deser, C., Phillips, A., Mai, A., Hannay, C., Strand, G., et al. (2015). The Community Earth System Model (CESM) Large Ensemble project: A community resource for studying climate change in the presence of internal climate variability, Bulletin of the American Meteorological Society, 96 (8), 1333-1349, https://doi.org/10.1175/BAMS-D-13-00255.1

Long. X., Newman, M., Shin, S.-I., Balmeseda, M., Callahan, J., Dusek, G., et al. (2025). Evaluating current statistical and dynamical forecasting techniques for seasonal coastal sea level prediction. Journal of Climate, 38(6), 1477–1503. https://doi.org/10.1175/JCLI-D-24-0214.1

Monahan, A. H., Fyfe, J. C., Ambaum, M. H. P., Stephenson, D. B., & North, G. R. (2009). Empirical Orthogonal Functions: The Medium is the Message. Journal of Climate, 22(24), 6501–6514. https://doi.org/10.1175/2009jcli3062.1

Newman, M. (2013). An empirical benchmark for decadal forecasts of global surface temperature anomalies. Journal of Climate, 26 (14), 5260-5269. https://doi.org/10.1175/JCLI-D-12-00590.1

Newman, M., Alexander, M. A. & Scott, J. D. (2011). An empirical model of tropical ocean dynamics. Climate Dynamics, 37, 1823-1841. https://doi.org/10.1007/s00382-011-1034-0

Newman, M. (2007). Interannual to decadal predictability of Tropical and North Pacific sea surface temperatures. Journal of Climate, 20(11), 2333-2356. https://doi.org/10.1175/JCLI4165.1

Penland, C., & Matrosova, L. (2006). Studies of El Niño and interdecadal variability in tropical sea surface temperatures using a nonnormal filter. Journal of Climate, 19(22), 5796-5815. https://doi.org/10.1175/JCLI3951.1

Penland, C., & Sardeshmukh, P. D. (1995). The optimal growth of tropical sea surface temperature anomalies. Journal of Climate, 8(8), 1999–2024. https://doi.org/10.1175/1520-0442(1995)008<1999:TOGOTS>2.0.CO;2

Rayner, N. A., Parker, D. E., Horton, E. B., Folland, C. K., Alexander, L. V., Rowell, D. P., et al. (2003). Global analyses of sea surface temperature, sea ice, and night marine air temperature since the late nineteenth century. Journal of Geophysical Research: Atmospheres, 108(D14), 4407. https://doi.org/10.1029/2002JD002670

Richter, K., Meyssignac, B., Slangen, A. B. A., Melet, A., Church, J. A., Fettweis, X., et al. (2020). Detecting a forced signal in satellite-era sea-level change. Environmental Research Letters, 15(9), 094079. https://doi.org/10.1088/1748-9326/ab986e

Robock, A. (1999). Volcanoes and climate. Reviews of Geophysics, 38(2), 191-219. https://doi.org/10.1029/1998RG000054

Rowell, D. P., Folland, C. K., Maskell, K., & Ward, M. N. (1995). Variability of summer rainfall over tropical north Africa (1906– 92): Observations and modelling. Quarterly Journal of the Royal Meteorological Society, 121, 669–704. https://doi.org/10.1002/qj.49712152311

Schmidt, E. (1907). Zur Theorie der linearen und nichtlinearen integralgleichungen. I Teil: Entwickelung willkürtlicher Funktionen nach Systemen vorgeschriebener. Mathematische Annalen, 63, 433-436.

Shin, S.-I., & Newman, M. (2021). Seasonal Predictability of Global and North American Coastal Sea Surface Temperature and Height Anomalies. Geophysical Research Letters, 48, e2020GL091886, https://doi.org/10.1029/2020GL091886

Solomon, A., & Newman, M. (2012). Reconciling disparate 20th century Indo-Pacific ocean temperature trends in the instrumental record. Nature Climate Change, 2, 691-699. https://doi.org/10.1038/nclimate1591

Solomon, A., & the US CLIVAR Decadal Predictability Working Group (2011). Distinguishing the roles of natural and anthropogenically forced decadal climate variability: Implications for prediction. Bulletin of the American Meteorological Society, 92(2), 141-156. https://doi.org/10.1175/2010BAMS2962.1

Strang, G. (2016). Introduction to Linear Algebra. 5th ed. Wellesley-Cambridge Press, Wellesley, MA, USA, 574 pp.

Sweet, W. V., Hamlington, B. D., Kopp, R. E., Weaver, C. P., Barnard, P. L., Bekaert, D., et al. (2022). Global and regional sea level rise scenarios for the United States: Updated mean projections and extreme water level probabilities along US coastlines. No. 01, NOAA Technical Report.

Ting, M., Kushnir, Y., Seager, R. & Li, C. (2009). Forced and internal twentieth-century SST trends in the North Atlantic. Journal of Climate, 22(6), 1469–1481. https://doi.org/10.1175/2008JCLI2561.1

Vautard, R., Yiou, P. & Ghil, M. (1992). Singular spectrum analysis: A toolkit for short, noisy chaotic signals, Physica D Nonlinear Phenomena, 58(1), 95-126. https://doi.org/10.1016/0167-2789(92)90103-T

von Storch, H., Bürger, G., Schnur, R., & von Storch, J.-S. (1995). Principal oscillation patterns: A review. Journal of Climate, 8(3), 377–400. https://doi.org/10.1175/1520-0442(1995)008<0377:POPAR>2.0.CO;2

Weare, B. C., & Nasstrom, J. S. (1982). Examples of extended empirical function analyses. Monthly Weather Review, 110(6), 481-485. https://doi.org/10.1175/1520-0493(1982)110<0481:EOEEOF>2.0.CO;2

Wills, R. C. J., Battisti, D. S., Armour, K. C., Schneider, T., & Deser, C. (2020). Pattern recognition methods to separate forced responses from internal variability in climate model ensembles and observations. Journal of Climate, 33(20), 8693-8719. https://doi.org/10.1175/JCLI-D-19-0855.1

Woodworth, P. L., & Player, R. (2003). The Permanent Service for Mean Sea Level. Journal of Coastal Research, 19(2), 287–295. https://www.jstor.org/stable/4299170

Zhang, X., & Church, J. A. (2012). Sea level trends, interannual and decadal variability in the Pacific Ocean. Geophysical Research Letters, 39(21), L21701. https://doi.org/10.1029/2012GL053240

Geophysical Research Letters

Supporting Information for

Estimating Global and Regional Sea Level Trends within the Recent Climate Record

Sang-Ik Shin[1,2], Cécile Penland[2]†, Matthew Newman[2], and Michael A. Alexander[2]

[1]University of Colorado/CIRES, Boulder, Colorado, USA

[2]NOAA/Physical Sciences Laboratory, Boulder, Colorado, USA

Corresponding author: Sang-Ik Shin (sangik.shin@noaa.gov)

†Retired

Contents of this file

Figures S1 to S3

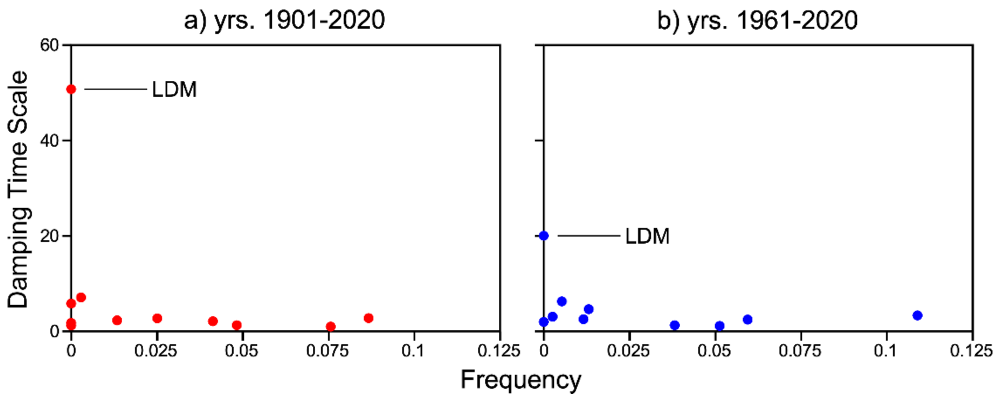

Figure S1. Comparison of the frequency and damping time scales of linear feedback matrix **L** derived using the SST anomalies during the period **a)** 1901-2020 and **b)** 1961-2020.

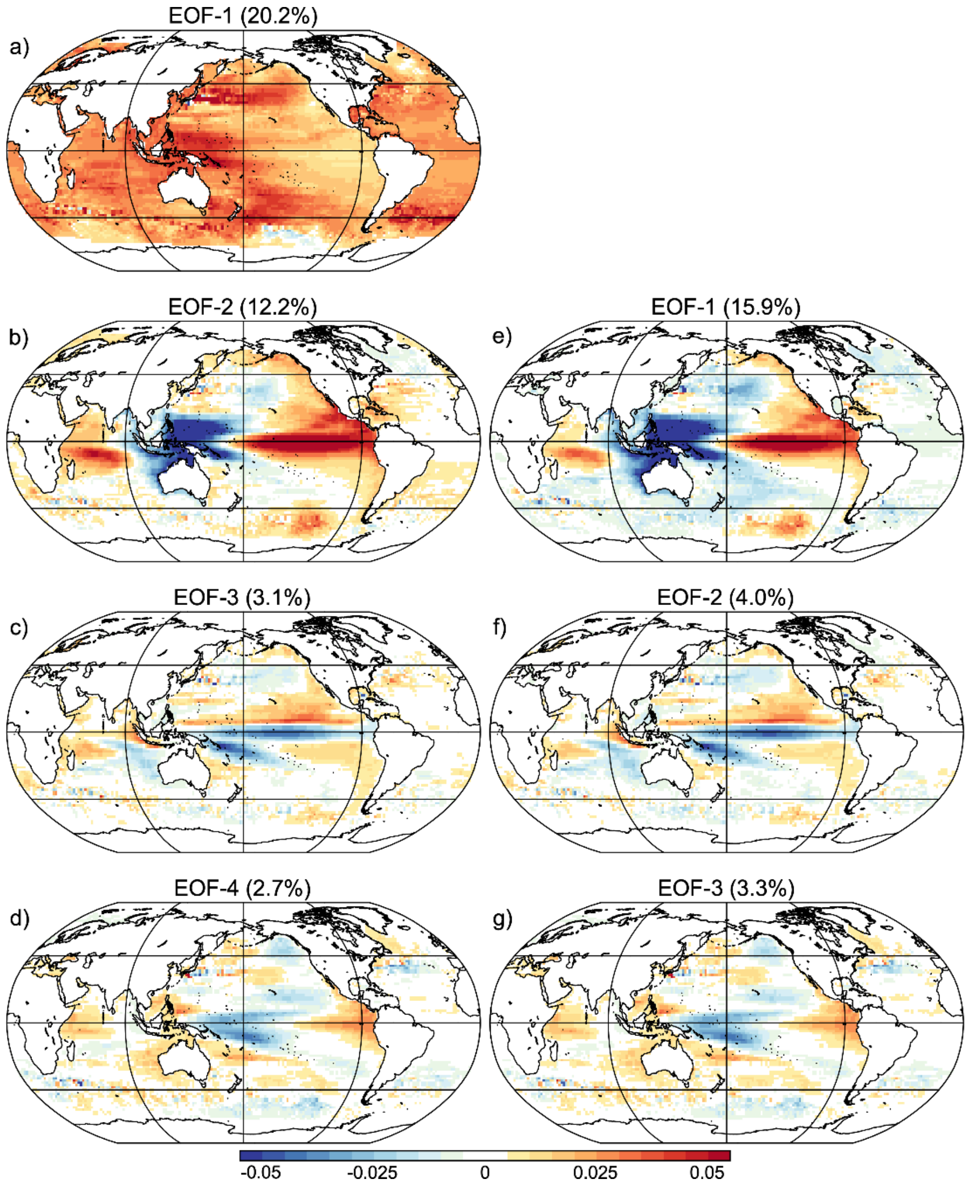

Figure S2. **a-d)** The leading 4 EOFs of SSH anomalies derived from the aviso dataset for 1993-2020. **e-g)** The leading 3 EOFs of SSH anomalies of which the externally-forced signals (see Fig. 4c) were filtered out using O-LDM.

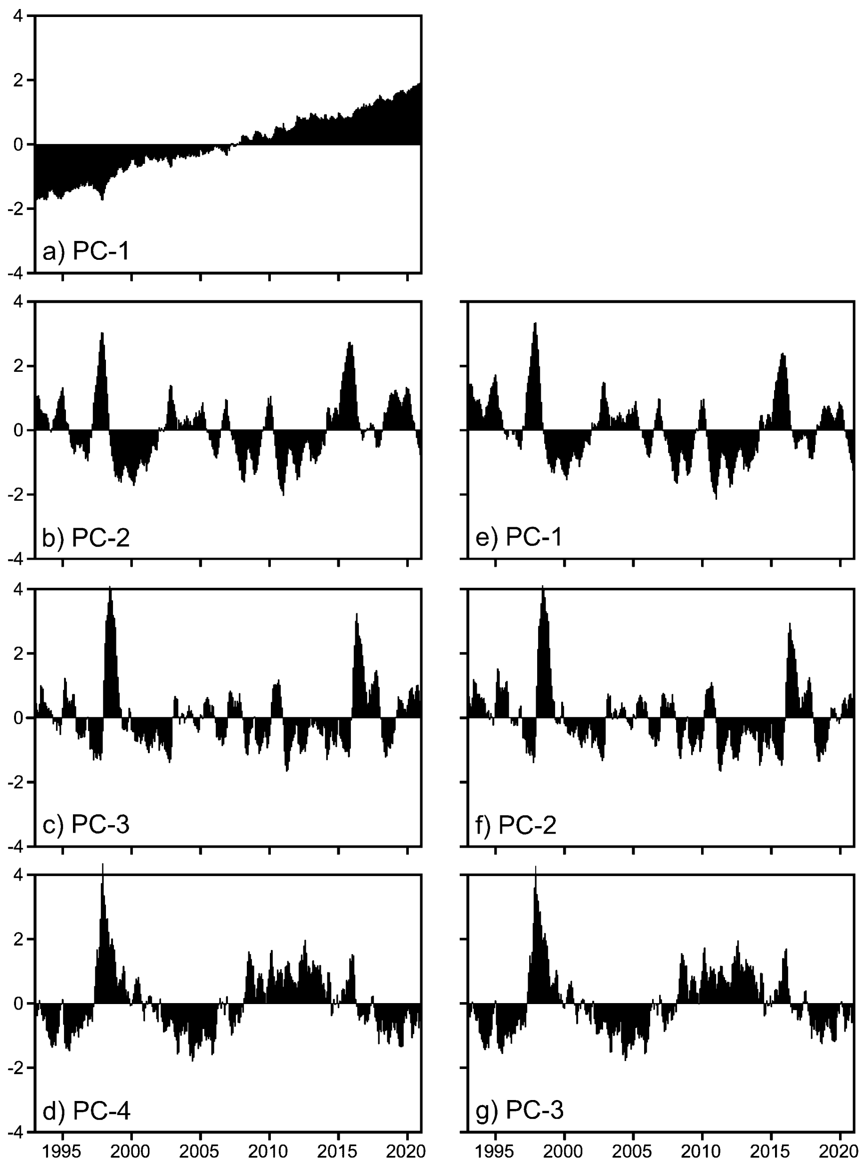

Figure S3. **a-d)** The accompanying 4 normalized PCs of SSH anomalies derived from the aviso dataset for 1993-2020 [EOFs are shown in Fig. S2a-d]. **e-g)** The accompanying 3 normalized PCs of SSH anomalies of which the externally-forced signals (see Fig. 4c) were filtered out using O-LDM [EOFs are shown in Fig. S2e-g].

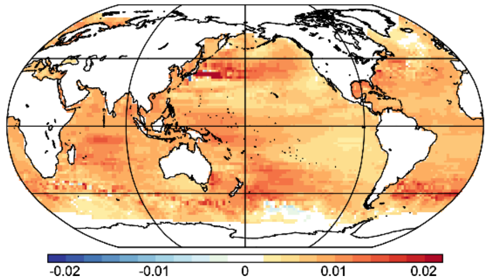

Figure S4. The difference between Fig. S2b and Fig. S2e.